Surface relief terraces in double-gyroid-forming polystyrene-block-polylactide thin films

Szu-Ming Yang , Jinwoo Oh , Benjamin R. Magruder , Hee Joong Kim , Kevin D. Dorfman , Mahesh K. Mahanthappa, and Christopher J. Ellison

Department of Chemical Engineering and Materials Science, University of Minnesota, Minneapolis, Minnesota 55455, USA



(Received 6 August 2023; accepted 17 October 2023; published 4 December 2023)

This study describes the thin film self-assembly behavior of a polystyrene-block-polylactide diblock copolymer, which undergoes melt self-assembly in bulk into a double gyroid (DG) network phase with a cubic unit cell parameter a = 52.7 nm. Scanning electron microscopy and grazing-incidence small-angle x-ray scattering reveal that thermally annealing 140-198 nm thick copolymer films on SiO₂ substrates below the morphological order-to-disorder transition temperature yields polydomain DG structures, in which the (422) planes are oriented parallel to the surface. Bright-field optical microscopy and atomic force microscopy analyses further reveal the film thickness-dependent formation of topographical terraces, including islands, holes, and bicontinuous features. The occurrence of these features sensitively depends on the incommensurability of the as-prepared film thickness with the (211)-interplanar spacing (d_{211}) of the DG unit cell. While the step heights between adjacent terraces exhibiting characteristic "double wave" patterns of the DG (422) planes coincide with d_{211} , previously unreported transition zones between adjacent terraces are observed wherein "boomerang" and "droplet" patterns are observed. These intermediate patterns follow the expected sequence of adjacent termination planes of the bulk DG unit cell along the [211] direction, as confirmed by comparisons with self-consistent mean-field theory calculations.

DOI: 10.1103/PhysRevMaterials.7.125601

I. INTRODUCTION

Ordered nanostructures arising from block copolymer (BCP) self-assembly in thin films have garnered substantial interest due to their technologically relevant microdomain topologies, tunable microdomain features across the $1-100\,\mathrm{nm}$ scale, and controllable domain orientations with respect to underlying substrates [1-4]. Depending on their molecular compositions, AB-type diblock copolymers self-assemble into one-dimensional (1D) lamellae, 2D hexagonally packed cylinders, and 3D micelle packings [5]. The thin film phase behaviors of such copolymers, in which the minority domains are discontinuous, have been extensively studied with attention to controlling their microdomain orientations with respect to the underlying substrate toward their application as soft templates for nanopatterning. BCPs also form 3D bicontinuous network phases with percolating and interpenetrating microdomain structures, such as the O^{70} and double gyroid (DG) phases. Triply continuous DG phases with Ia3d symmetry [6], which comprise two oppositely handed and interpenetrating nanochannel networks situated in a matrix with specific unit cell dimensions, have garnered particular interest as photonic crystals [7,8], optical metamaterials [9–11], size-selective separation membranes

Published by the American Physical Society under the terms of the Creative Commons Attribution 4.0 International license. Further distribution of this work must maintain attribution to the author(s) and the published article's title, journal citation, and DOI.

[12], and components in hybrid solar cells [13,14]. Although these applications depend primarily on thin films of these copolymers, the thin film phase behaviors of DG-forming BCPs remain much less well-studied.

While the thermotropic self-assembly of two-component (A/B) BCPs depends principally on the copolymer volume composition ($f_A = 1-f_B$), the total degree of polymerization (N), and the temperature-dependent effective interaction penalty for A/B monomer contacts (χ) [15,16], their phase behaviors in thin films supported on various substrates are substantially more complex. Surface field effects, arising from interactions between the homopolymer-rich microdomains and the adjoining surfaces, often drive local microdomain orientation and the local BCP film composition to maximize favorable contacts and minimize overall free energy. For example, a surface field that preferentially wets one segment typically directs thin films of lamellae- and cylinder-forming BCPs to orient their microdomains parallel to the underlying surface. The spatial confinement additionally imposed by the thin film geometry, which is often quantified as the ratio of the film thickness (t) normalized by the bulk unit cell dimensions (L_0) , can also drive new morphological behaviors [17–21]. In films of incommensurate thickness subject to surface fields, i.e., noninteger t/L_0 , the BCP nanostructure often minimizes its free energy by either: (1) distorting to a nonbulk domain spacing by uniform domain swelling or compression or by unit cell distortion, or (2) forming terraced film morphologies consisting of islands, holes, and bicontinuous structures, with terrace heights that are integer multiples of L_0 [22]. Since uniform swelling of the microdomains requires entropically unfavorable polymer chain stretching, terrace formation with L_0 -quantized thicknesses is often thermodynamically

^{*}Corresponding author: cellison@umn.edu

preferred [3]. On the other hand, surface terrace formation typically does not occur in BCP thin films with commensurate thicknesses (integer values of t/L_0).

Coulon et al. first observed film thickness quantization in L_0 multiples for lamellar polystyrene-block-poly(methyl methacrylate) thin films after thermal annealing [23], and van Dijk et al. discovered related thickness quanta ("hills and valleys") in cylinder-forming polystyrene-block-polybutadieneblock-polystyrene thin films [24]. While these seminal studies considered adjoining surface fields that preferentially directed microdomain orientation parallel to the film surfaces, BCP confinement between neutral surfaces that do not preferentially wet either copolymer segment can yield perpendicularly-oriented lamellar and cylindrical morphologies absent any surface terracing [25]. Since surface relief terraces often appear in lamellae- [26,27], cylinder- [28,29], and sphere-forming [30] BCP thin films, the factors leading to these features have been studied as a function of specific surface fields [21,31–33], film thickness [19,27,34], and annealing conditions [27,35]. Importantly, the "transition zones" that separate higher and lower terraces in a BCP thin film often reveal important insights into how terracing is accommodated, especially, since the morphology and its orientation may significantly differ from the surrounding terraces.

In this study, we characterize previously unreported terrace formation in bicontinuous DG network morphologies of model polystyrene-block-polylactide (SL-G) BCP thin films. Consequently, this report addresses the outstanding question of how network-forming thin films accommodate terrace formation, as compared to well-studied lamellar, cylindrical, and spherical morphologies. By using simple thermal annealing protocols, (211)-oriented DG thin films displaying characteristic (422) termination planes parallel to the air surface were prepared. Uniform and terraced SL-G thin films were observed depending on the as-prepared average film thickness (t_{avg}) and annealing temperature. Film morphologies and their unit cell orientations were evaluated using brightfield optical microscopy (OM), scanning electron microscopy (SEM), atomic force microscopy (AFM), and 2D grazingincidence small-angle x-ray scattering (GISAXS). Thus, this work bridges existing results for terrace formation in classical spherical, cylindrical, and lamellar block copolymer morphologies comprising discontinuous microdomains with that of bicontinuous networks with interpenetrating and percolating microdomain topologies.

II. EXPERIMENTAL SECTION

Synthesis and characterization of hydroxyl-terminated polystyrene (PS-OH) and hydroxyl-terminated polystyrene-block-polylactide (PS-PLA-OH). This synthesis follows a previously reported procedure [36] that is depicted in Fig. S1 (see Supplemental Material [37]). Briefly, PS-OH was synthesized by anionic polymerization of styrene, an end-capping reaction to add a single ethylene oxide unit, and subsequent termination with and precipitation into CH₃OH. This PS-OH then served as a macroinitiator for the ring-opening polymerization (ROP) of D,L-lactide catalyzed by stannous (II) 2-ethylhexanoate (Sn(Oct)₂). After vacuum drying of the PS-OH at 40 °C for \geqslant 48 h, PS-OH, D,L-lactide and Sn(Oct)₂

were codissolved in anhydrous toluene in 50-mL pressure vessel in a glovebox. ROP was conducted at 100 °C for 20 h, after which the reaction was stopped by immersion in a dry ice/methanol bath. The resulting copolymer product was precipitated into CH₃OH, and the PS-PLA-OH was collected by vacuum filtration.

Proton nuclear magnetic resonance (^{1}H NMR) spectroscopy in CDCl₃ at 22 °C was performed on a Bruker Avance III HD spectrometer operating at 400 MHz, with ^{1}H chemical shifts reported in parts per million (ppm) relative to the residual protiated solvent signal ($\delta = 7.26$ ppm). From the quantitative ^{1}H NMR spectra for PS-OH and PS-PLA-OH given in Fig. S2 and S4 (see Supplemental Material [37]), the volume fraction of PLA block in PS-PLA-OH was determined to be $f_{\rm PLA} = 0.51$, based on integrated peak areas associated with signals at $\delta = 5.2$ and 6.8, the molecular weights of the repeat units in each block ($MW_{\rm styrene} = 104$ g/mol, $MW_{\rm lactide} = 72$ g/mol), and the melt homopolymer densities of PS and PLA at 110 °C ($\rho_{\rm PS} = 1.02$ g/cm³ and $\rho_{\rm PLA} = 1.18$ g/cm³) [36].

Absolute molecular weights and molecular weight dispersities $(D = M_w/M_n)$ of the PS-OH macroinitiator and PS-PLA-OH were determined by size-exclusion chromatography (SEC). These analyses employed an Agilent Infinity 1260 HPLC running with HPLC grade tetrahydrofuran (THF) at an elution rate of 1 mL/min, which was equipped with three Waters Styragel HR columns (300 mm length, 7.8 mm diameter), a Wyatt DAWN HELEOS-II 18-angle static light scattering (LS) detector, and a Wyatt Optilab T-rEX differential refractive index detector. Absolute molecular weight determination assumed 100% mass recovery in the chromatographic separation. Since LS typically underestimates the value of D, we used SEC with a conventional calibration curve constructed using narrow dispersity polystyrene standards (Agilent Easi-Cal PS Standards) [38]. The latter analyses were conducted using a Viscotek GPCMax VE 2001 system running in HPLC grade THF with an eluent flow rate of 1 mL/min, which was equipped with two Agilent Technologies PLGel Mixed-B columns (350 mm × 7.5 mm), a Viscotek VE 3580 refractive index (RI) detector. Both analyses relied on samples prepared with concentrations of 2-4 mg polymer/mL THF. SEC traces of PS-OH ($M_n = 7.7 \text{ kg/mol}$, D = 1.1) and PS-PLA-OH ($M_{n,total} = 16.7 \text{ kg/mol}, D = 1.6$) are given in Fig. S5 (see Supplemental Material [37]).

The thermal properties of PS-PLA-OH were characterized by differential scanning calorimetry (DSC) and thermogravimetric analysis (TGA). DSC measurements were conducted using a Mettler Toledo DSC1 instrument under a nitrogen atmosphere. The temperature ramp rate was set to 10 °C/min, and both the first and second heating cycles scanned temperature from 30 °C to 200 °C. Glass transition temperatures of the PS block $(T_{g,PS} = 88 \,^{\circ}\text{C})$ and the PLA block ($T_{g,PLA} = 51$ °C) were determined from the second heating cycle (see Fig. S6 [37]), suggesting the microphase separation of this copolymer. Dynamic TGA measurements were performed on a TA Instruments Q500 operating with a nitrogen gas flow rate of 100 mL/min and a ramp rate of 10 °C/min. PS-PLA-OH was found to be thermally stable (< 2 wt%) at or below 180 °C (see Fig. S7 [37]).

Synthesis and characterization of acetylated PS-PLA (SL-G). To minimize both degradation of PS-PLA-OH during thermal annealing and grafting reactions of the hydroxyl endgroup to native oxide surface on the silicon wafers, a chemical end-capping reaction was performed [39] on PS-PLA-OH after vacuum drying for at least 48 h (see Fig. S3 for the reaction scheme [37]). In an oven dried, 100 mL 3-necked flask, PS-PLA-OH and 10 molar equivalents of 4dimethylaminopyridine (DMAP) were dissolved in anhydrous dichloromethane (CH₂Cl₂). After sealing the reactor ports with rubber septa, the reactor was cooled to 0 °C in an ice bath. The reactor contents were degassed by sparging with Ar(g)for ≥30 min, prior to dropwise addition of 10 molar equivalents of acetyl chloride dissolved in anhydrous CH₂Cl₂. After 30 min at 0 °C, the reaction was warmed to ambient temperature and allowed to stir for another 2.5 h. The resulting product was then precipitated into CH₃OH. After adding a small amount of deionized water to the solution to facilitate dissolution of the DMAP-hydrochloride salt reaction byproduct, this solution was stirred overnight. The acetyl-terminated PS-PLA (SL-G) was collected by vacuum filtration and subsequently dried at 40 °C under vacuum for \geq 48 h.

NMR, SEC, DSC, and TGA analysis of SL-G are summarized in Figs. S4–S7 using the above methods (see Supplemental Material [37]). The disappearance of the $^1\mathrm{H}$ NMR resonance at $\delta=4.3$ ppm corresponding to the methine hydrogen of the PLA-CH(CH₃)-OH endgroup indicates the success of the end-capping reaction. SEC analyses indicate that $M_{\rm n}=16.7$ kg/mol and D=1.6, which are unchanged relative to the PS-PLA-OH precursor, while DSC reveals that the $T_{\rm g,PS}=89$ °C and $T_{\rm g,PLA}=52$ °C for SL-G are like those of PS-PLA-OH. Notably, SL-G exhibits greater thermal stability in dynamic TGA analyses. In isothermal TGA analyses (nitrogen gas flow rate 100 mL/min) relevant to thin film annealing studies conducted in this study, SL-G exhibits < 0.5 wt% loss over 100 min.

The bulk morphology of SL-G thermally annealed at 180 °C was examined by SEM and transmission small-angle x-ray scattering (T-SAXS). To enhance contrast between the microdomains, the PLA block was in some cases selectively removed by chemical etching of the sample by immersion in 0.1 M NaOH in 50:50 v/v CH₃OH/H₂O for 10 min [40]. SEM was performed on a Hitachi SU8230 using secondary electron detection with a working distance of 4 mm and accelerating voltage of 1.5 kV. A representative SEM image of a chemically etched, bulk SL-G sample shown in Fig. S8(a) indicated its assembly into a DG phase (see Supplemental Material [37]). T-SAXS measurements were performed on a SAXSLAB Ganesha instrument at ambient temperature under vacuum. The instrument was equipped with a Cu K_{α} X-ray microsource, two scatterless collimating apertures, and Eiger 1M (Dectris) detector (79.9 mm x 77.2 mm active area) that was calibrated using a silver behenate standard (d = 58.38 Å). In the representative T-SAXS pattern of the unetched, bulk SL-G sample given in Fig. S8(b), the diffraction peaks occur at $(q/q^*)^2 = 6$, 8, 16, and 22 consistent with the expected reflections for the cubic $Ia\bar{3}d$ symmetry (space group 230) of the DG phase (see the Supplemental Material [37]). Since the first SAXS peak located at $q = 0.0292 \text{ Å}^{-1}$ corresponds to the (211) reflection of the DG unit cell, the interplanar (211) spacing is $d_{211} = 21.5$ nm and the unit cell parameter $d_{100} = 52.7$ nm.

Preparation and characterization of SL-G thin films. Si wafers covered with a ~2 nm-thick native oxide were sequentially cleaned with acetone, methanol, and ethanol using bath sonication at ambient temperature. Solutions with SL-G concentrations of 20-40 mg polymer/mL toluene were spincoated onto the cleaned Si wafers at 1500 to 2500 rpm to prepare thin films of varied thicknesses. After residual solvent removal by annealing at 110 °C for 10 s, the as-cast SL-G thin films thicknesses were measured using an M-2000V ellipsometer (J.A. Woollam Co.) with source wavelength range of 370 to 1000 nm (390 wavelengths) at three different incident angles (55°, 65°, 75°) and by direct AFM height profile analyses (vide infra). Details of the thickness measurements are described in the supporting information (see Fig. S10 [37]). The SL-G thin films were then thermally annealed at 180 °C for 1 min under vacuum to form polydomain DG thin films. To facilitate imaging, DG thin films were irradiated with UV light (Omnicure S1500, 200 W mercury arc lamp which irradiates light of wavelengths from 320 to 500 nm, 100 W/cm², 10 mins) to lightly crosslink the PS domains to mitigate unintended reconstruction of the film morphology during PLA removal. The PLA block was then selectively etched by immersion 0.1 M NaOH in 50:50 v/v CH₃OH/H₂O for 10 min. The thin films were then rinsed with deionized water and dried under a nitrogen gas stream. The procedure is schematically depicted in Fig. S9 (see the Supplemental Material [37]).

SL-G thin films were characterized by OM, SEM, AFM, and GISAXS measurements. OM imaging was performed on a Nikon Eclipse E200. AFM imaging was conducted using a Bruker Nanoscope V in tapping mode, stabilized in the repulsive regime. AFM Tips (HQ:NSC36/AL BS, force constant = 2 N/m, resonance frequency = 130 kHz) were purchased from MikroMasch USA, and AFM images were analyzed using freely available Gwyddion software for scanning probe microscopy data visualization.

GISAXS measurements were performed at the 8-ID-E beamline of the Advanced Photon Source (Argonne National Laboratory, IL, USA). GISAXS patterns of unetched SL-G thin films were measured at an incident angle of 0.14° using an incident beam energy of 0.915 keV and sample-to-detector distance of 2183.4 mm. The 2D GISAXS data were analyzed using GIXSGUI 1.7.3 [41]. The unit cell parameters of DG formed by SL-G thin films were calculated by minimizing the error $\Delta q/q_{\rm obs} = (q_{\rm obs} - q_{\rm calc})/q_{\rm obs}$ between positions of the observed scattering peaks (q_{obs}) and the calculated scattering peaks (q_{calc}) of the thin film samples. A slight distortion of the DG unit cell was observed in the thin films, evidenced by the observation of an unexpected, weak low q peak. Since this peak corresponds to the (110) reflection of a DG with a modest triclinic distortion (vide infra), this space group was used in the GISAXS reported analyses.

Microstructure prediction based on self-consistent field theory (SCFT) calculation. The 3D composition profile and 2D contour plots of the DG phase were generated using a converged solution from SCFT, calculated with the PSCF software tool [42] using $64 \times 64 \times 64$ resolution and a minority block volume fraction $f_A = 0.4$ with a segregation strength $\chi N = 20$. This converged solution represents the

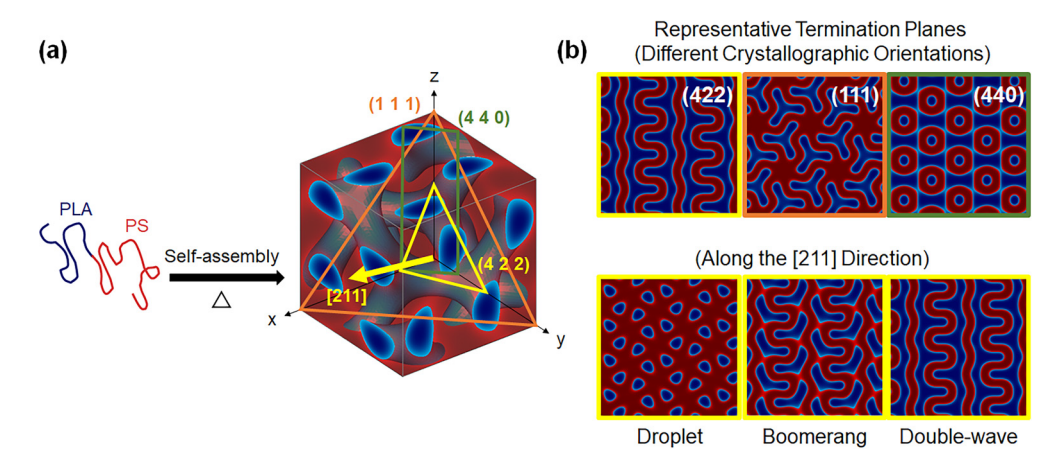


FIG. 1. (a) Schematic depiction of SL-G self-assembly into a cubic DG structure, in which the PLA (*blue*) forms two enantiomeric, interpenetrating cable networks within the PS matrix (*red*). The (422), (111), and (440) planes (marked as yellow, orange, and green, respectively) are shown in the DG unit cell. (b) Representative termination planes for different crystallographic orientations of DG derived from a converged DG solution from self-consistent field theory (SCFT), and "droplet", "boomerang", "double-wave" patterns found on different termination planes along the [211] direction.

equilibrium bulk morphology of the DG microdomains in a unit cell with periodic boundary conditions. The 2D contour plots show the domain patterns found on slices through the bulk unit cell, and do not represent any domain distortion that may occur at a polymer-substrate or polymer-air interface. The visualizations were generated in MATLAB using the Polymer Visual tool [43].

III. RESULTS AND DISCUSSION

The model SL-G copolymer system employed in this study was selected based on literature precedents related to the ease of its synthesis by tandem anionic and ring-opening polymerizations [36], and the chemical etchability of the PLA segments for high contrast imaging. Note that the SL-G copolymer used in these studies bears a hydrocarbyl endgroup at the PS terminus and an acetyl endgroup at the PLA segment terminus. This fact minimizes the possibility of thermally-induced polymer decomposition reactions in films annealed for ≤100 min based on TGA analyses presented in Fig. S7 (see Supplemental Material [37]). The presence of these end groups also eliminates the possibility of thin film phase behavior artifacts stemming from polymer grafting reactions to the native oxide present on the Si substrate during short, high temperature annealing steps.

Molecular design of the network-forming SL-G copolymer was further guided by reports of the bulk and thin film phase behaviors of PS-PLA diblocks. Prior work by Hillmyer and coworkers established that narrow dispersity PS-PLA diblocks and their blends form bulk DG phases in a narrow phase window spanning $f_{\rm PLA} = 0.40-0.42$ [36,44]. On the other hand, Chen *et al.* [45] and Olayo-Valles *et al.* [25] demonstrated that the BCP/vacuum interface is non-preferential (neutral) for lamellae-forming PS-PLA thin films with nearly symmetric compositions $(0.50 \le f_{\rm PLA} \le 0.53)$ for samples thermally annealed at $T = 150-180\,^{\circ}$ C. Note that this observed neutrality is a function of the interaction between individual repeat units with the adjoining vacuum surface and the relative proportion of each repeat unit type

present in the block copolymer, which depends on the copolymer chemical composition [46,47]. In the present work, we sought to exploit these collective findings by generating DGforming BCPs at nearly symmetric compositions to eliminate the need for surface modifying "topcoat" layers [48] to maintain surface neutrality. Such a molecular design requires a means for shifting the DG phase window location to higher values of f_{PLA} . Prior literature [49,50] established that judicious introduction of molecular weight dispersity into one segment of a diblock copolymer can affect exactly the desired morphology window shift. Thus, we found that broadening the molecular weight dispersity of PLA segment in SL-G such that $D_{SL-G} = 1.6$ and $D_{PS} = 1.1$ drives interfacial curvature toward the PLA microdomain to promote DG formation at $f_{\rm PLA} = 0.51$ with a cubic lattice parameter $L_0 = 52.7$ nm as determined by lab-source T-SAXS measurements (see Fig. S8 [37]).

Figure 1(a) schematically depicts the self-assembly of SL-G into a DG morphology. In this microphase separated structure, PLA comprises the interpenetrating networks of cables (blue), and PS forms the matrix (red). The geometric complexity of the DG network results in the presentation of distinct domain patterns on different crystallographic planes of the unit cell, which can be matched to the experimentally visible termination planes at the top surface of a thin film to unambiguously identify the DG unit cell orientation relative to the substrate. To illustrate this point, Fig. 1(b) provides SCFT solutions of representative termination planes of different lattice orientations. For example, (422) planes exhibit periodic "double-wave" patterns, (111) planes display "tripodlike" patterns, and (440) planes yield hexagonal "doughnutlike" patterns. These distinct termination plane patterns have been previously observed in solvent-annealed DG thin films [51]. Additionally, different termination planes can be observed for a single lattice orientation because the domain patterns on a crystallographic plane vary as the plane is moved along its corresponding direction (the plane normal vector). There are three main types of structural patterns along the [211] direction as shown in Fig. 1(a), including "droplet",

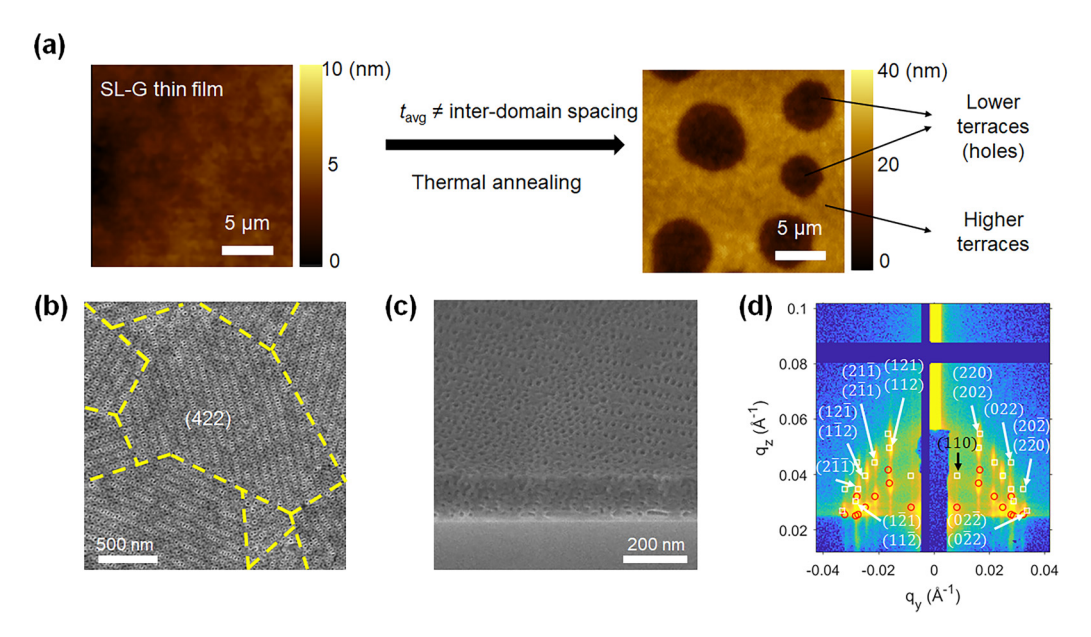


FIG. 2. (a) AFM images of a SL-G thin film before and after thermal annealing with $t_{\text{avg}} = 165 \text{ nm} = 7.7 d_{211}$, in which lower terraces ("holes") form. (b) Top-view SEM image of a polygrain SL-G thin film after PLA removal by chemical etching, showing the characteristic (422) plane with "double-wave" termination. (c) Birds-eye view SEM image (60° tilted) of the etched polygrain SL-G thin film showing that the DG structure persists throughout the film thickness. (d) 2D-GISAXS pattern for this terraced polygrain SL-G thin film, wherein the calculated reflected and transmitted peaks are respectively marked with white squares and red circles based on the lattice constants a = 49.0 nm, b = c = 52.0 nm, $\alpha = 93^{\circ}$, $\beta = \gamma = 94^{\circ}$.

"boomerang" and "double-wave" patterns [Fig. 1(b)]. The (211) orientation has been often reported to preferentially orient parallel to the substrate by tailoring the surface energy of the interfaces or using specific thermal or solvent annealing conditions [51–53]. Although the full scope of termination plane and unit cell orientation selection is still unclear, a recent study has suggested that the relative areal fractions of DG domain terminations presented to interfaces combined with their respective interfacial contact energies that can be modulated by solvent content could be important [51].

To understand the thin film properties of SL-G, films were prepared on clean Si wafers covered with native oxide. The average film thickness (t_{avg}) was precisely controlled $(\sim \pm 1-2 \text{ nm})$ by the manipulating the solution spin-coating speed and concentration of the copolymer solution. Figure 2(a) shows AFM images of a SL-G thin film with average thickness $t_{avg} = 165$ nm before and after thermal annealing at 180 °C under vacuum for 1 min. Although the root-meansquare (r.m.s.) roughness of the as-cast SL-G thin film prior to annealing is < 1 nm, high temperature annealing results in the formation of substantial surface relief terraces. Lower terraces ("holes") 20 ± 1 nm in depth and $5-20 \,\mu m$ in lateral dimension formed after thermal annealing. Figure 2(b) shows a representative top-view SEM image of the higher terrace portion in the same film. The characteristic "doublewave" pattern of the (422) termination plane is present at the top surface, as observed in other studies of DG thin films [52–54]. (211)-oriented polygrain structures were obtained by thermally annealing at 180 °C, whereas lower annealing temperatures resulted in mixed DG termination planes at the film surface or poorly resolved surface features (see Fig. S11 [37]). The term "polygrain" indicates that the propagation direction of the "double-wave" pattern is different for each grain with distinct grain boundaries observed at the top surface [demarcated by yellow dashed lines in Fig. 2(b)]. While previous research has shown that DG-forming BCP thin films form structures that depend on the average film thickness [54,55], terraced structures have not been previously reported. Based on the SL-G DG lattice constant $L_0 = 52.7$ nm, we note that the $t_{\text{avg}} = 3.1L_0$ or $7.7d_{211}$ for this film is incommensurate with both the DG lattice constant and the (211) interplanar spacing.

To further confirm that the hole features in Fig. 2(a) were formed by the DG phase, the surface and through film morphology of the SL-G thin films were characterized by SEM and 2D-GISAXS. Figure 2(c) shows a representative bird'seye view SEM image of the annealed SL-G thin film. A 3D DG network structure apparently persists through the entire depth of the SL-G film, inside the holes and elsewhere, with no observed formation of other morphologies or wetting layers. A representative 2D-GISAXS pattern of an unetched, (211)-oriented, polygrain SL-G thin film with $t_{avg} = 165 \text{ nm}$ is shown in Fig. 2(d), where q_z and q_y respectively denote the scattering wave vectors along the substrate normal (outof-plane) and substrate parallel (in-plane) directions. The measurement angle of incidence $a_i = 0.14^{\circ}$ was specifically selected to be greater than the critical angle (a_c) of the SL-G thin films, thus enabling measurement of the internal structures through the entire depth of the film. The peaks arising from the beam reflected and transmitted through these thin films separate vertically in the 2D-GISAXS pattern, and their calculated peak positions are respectively marked with white squares and red circles. The clearly resolved {211} and {220} diffraction peaks in Fig. 2(d) confirm the (211) orientation of the DG thin film [56]. However, these patterns also exhibit an unexpected low q diffraction peak corresponding to

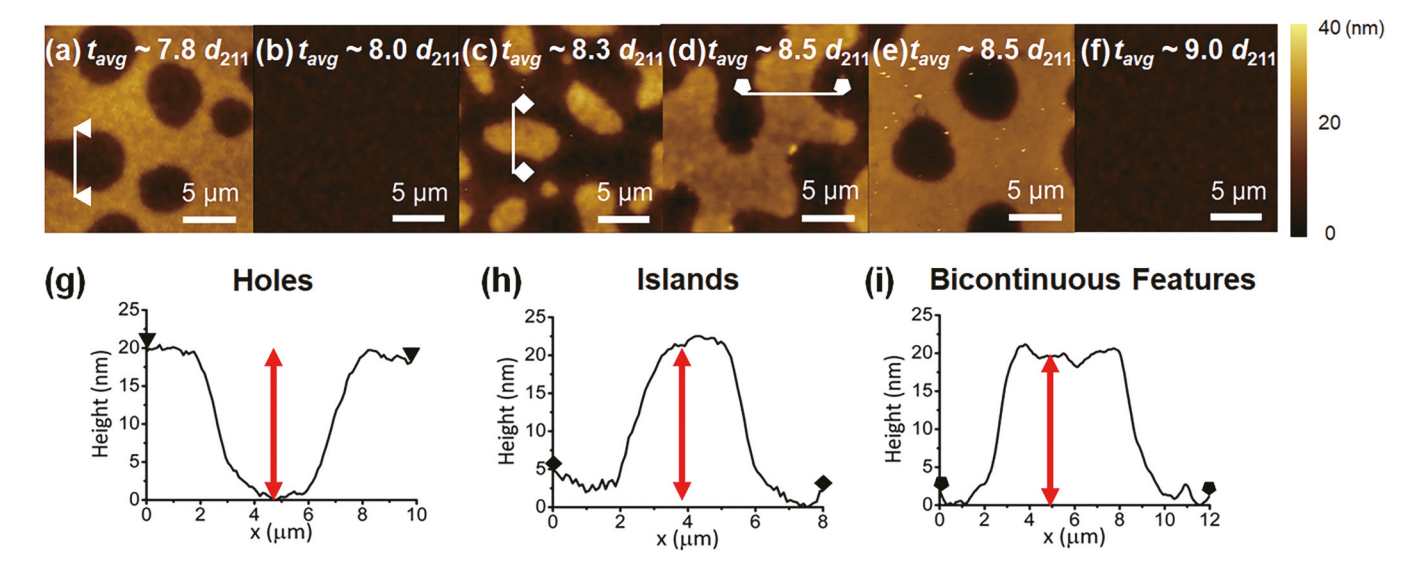


FIG. 3. (a)–(f) AFM images of SL-G thin films with average thickness ranging from 168 nm $(7.8d_{211})$ to 193 nm $(9.0d_{211})$, illustrating the formation of flat (featureless) films when $t_{\rm avg}$ is an integer multiple of d_{211} and terrace formation otherwise. (g) Height profile of holes along the line scan depicted in panel (a). (h) Height profile of islands along the line scan indicated in panel (c). (i) Height profile of bicontinuous features along the line scan drawn in panel (d). The heights of different types of terraces, represented by the red double arrows, were approximately equal to the value of $d_{211} = 21.5$ nm.

a {110} reflection that is not anticipated for the for Ia3d symmetry. This characteristic indicates that the DG network in the thin film breaks cubic symmetry in a nonaffine manner, such that the unit cell becomes distorted by virtue of thin film confinement. Lattice distortion of the DG unit cell in BCP thin films has also been observed in prior work [56–58], and has been ascribed to film deswelling behavior after solvent vapor annealing. It is possible that the unit cell distortions in the present work could be similarly due to solvent removal during spin coating, but deeper inquiry of this phenomenon is beyond the scope of this study. Nonetheless, previously reported GISAXS analyses demonstrated that contraction of a (211)-oriented DG unit cell primarily along the substrate normal drives cubic lattice symmetry breaking to form a triclinic crystal with lattice parameters $a \neq b = c$ and angles $\alpha \neq \beta =$ γ [58]. The unit cell parameters of DG SL-G thin films were fit by matching the calculated scattering peak positions for triclinic lattice with space group $P\bar{1}$ with the experimentally observed GISAXS peaks. The resulting lattice parameters are $a = 49.0 \text{ nm}, b = c = 52.0 \text{ nm}, \alpha = 93^{\circ}, \text{ and } \beta = \gamma = 94^{\circ}$ for the polygrain SL-G thin film, consistent with primarily unidirectional distortion along the substrate normal direction. The remainder of this manuscript will discuss the system in the context of an undistorted unit cell for simplicity.

We now examine more closely the terraced morphologies of the SL-G thin films as a function of the average film thickness $140 \leqslant t_{\rm avg} \leqslant 193$ nm spanning the range $t_{\rm avg} = 6.5 d_{211}$ to $9.0 d_{211}$. Upon annealing these films at $180\,^{\circ}{\rm C}$ under vacuum for 1 min, 2D-GISAXS patterns for films with $t_{\rm avg} < 7.0 d_{211}$ exhibit coexisting hexagonally packed cylinders and DG morphologies (see Fig. S12 [37]). On the other hand, thicker films with $7.0 d_{211} < t_{\rm avg} < 9.0 d_{211}$ formed polygrain (211)-oriented DG phases as confirmed by GISAXS and SEM analyses. To investigate the terraces formed by these (211)-oriented DG thin films, representative AFM and SEM images of SL-G thin films with different average thickness are shown

in Figs. 3(a)–3(f) and Fig. S13 (see the Supplemental Material [37]), respectively.

Figure 3 shows that the types of surface relief terraces, including holes, islands, and bicontinuous features, depend on the average film thickness and that $d_{211} = 21.5$ nm is a critical parameter that influences terrace formation. We discovered that when t_{avg} is commensurate with the d-spacing between adjacent (211) planes of the DG unit cell (i.e., $t_{avg}/d_{211} = n$ is an integer > 7), no terraces form in the SL-G thin film [Figs. 3(b) and 3(f)]. On the other hand, when t_{avg} is incommensurate with d_{211} , (211)-oriented DG films spontaneously form terraced islands or holes by locally modulating film thickness on annealing. There are two different scenarios: (1) holes are typically observed when $(n-0.5) < t_{avg}/d_{211} < t_{avg}/d_{211}$ n, and (2) islands typically form when $n < t_{avg}/d_{211} < t_{avg}/d_{211}$ (n + 0.5). Bicontinuous surface features are observed at the transition between island and hole terraces $(t_{\rm avg}/d_{211} \sim n +$ 0.5). The total areal fraction of islands or holes is expected to depend on average thickness because the total mass of the BCP must be conserved as these structures form (see OM images in Fig. S14 [37]). Based on the representative SEM images shown in Fig. S13, the polygrain characteristic (422) termination plane or "double-wave" pattern is observed in both lower and higher terrace regions (see the Supplemental Material [37]).

Binder *et al.* argued that the terrace formation is analogous to macrophase separation via spinodal decomposition in polymer blends [59]. BCP thin films spontaneously develop terraces with certain step heights, allowing the termination plane on each terrace to be that which exhibits the lowest excess free energy at the polymer-air interface, while maintaining an internal structure with the same periodicity as the bulk morphology. The height profiles of three types of surface relief terraces are shown in Fig. 3(g)-3(i). The step heights of holes, islands, and bicontinuous features are all 20 ± 1 nm, strikingly similar to d_{211} . This result may be

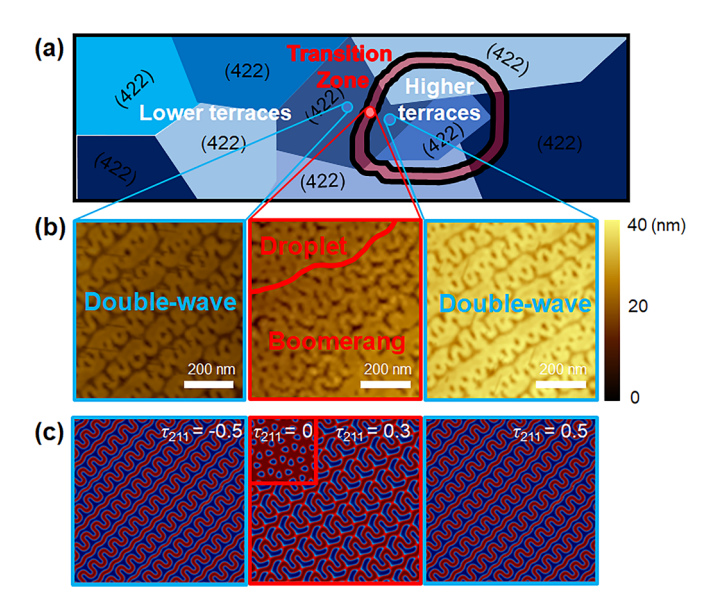


FIG. 4. (a) Top-view schematic of polygrain SL-G thin film after thermal annealing identifying the transition zone ($red\ region$). (b) AFM images of the terraces and transition zone formed in an SL-G thin film with $t_{avg}=198\ nm\ (9.2d_{211})$ after thermal annealing and removal of PLA by chemical etching. The remaining PS phase (yellow) in different termination planes along the [211] direction were readily observed by AFM. (c) SCFT solutions of representative crystallographic planes with varied τ_{hkl} along the [211] direction match with the experimentally observed surface features in panel (b).

explained by visualizing the different termination planes along the [211] direction in the DG unit cell (see Fig. S15 [37]). A termination coordinate parameter, τ_{hkl} , was used to represent the distance from the crystallographic origin to the termination plane along a certain direction in units of structural periodicity [60]. τ_{hkl} is defined as

$$\tau_{hkl} = \frac{x}{a} \sqrt{h^2 + k^2 + l^2},$$

where x is the distance from the plane (hkl) to the termination plane along the [hkl] direction and a is the lattice parameter of the cubic unit cell, such that the termination coordinates $\tau=0$ and $\tau=1$ are identical. For example, (211)-oriented DG with $\tau_{211}=0.5$ exhibits (422) termination planes. In SL-G thin films with surface relief terraces, the "double-wave" (422) pattern could be observed at both the lower and higher terraces. The height difference between two identical "double-wave" surfaces on adjacent terraces should thus be equal to d_{211} , not d_{422} . Therefore, 20 ± 1 nm step-heights of the different types of surface relief terraces in (211)-oriented SL-G thin films match the expected d_{211} distance between adjacent "double-wave" patterns.

To further understand the structural details of terrace formation, a (211)-oriented SL-G thin film with islands ($t_{avg} = 198 \text{ nm} = 9.2d_{211}$) was imaged by AFM. Figure 4(a) shows a top-view schematic of a polygrain (211)-oriented SL-G thin film after thermal annealing. Notably, a single DG grain is observed to be continuous across the region between the lower and higher (islands) terraces (similar to the SEM images in Fig. S13 [37]), suggesting that the formation of

grain boundaries across the transition zone is not required. In a grain that is continuous across a step height, structural patterns other than the "double-wave" were often observed in between the terraces. For convenience, we identify these region with structural features other than "double-wave" in between the terraces as the "transition zone" indicated in red in Fig. 4(a). Figure 4(b) shows AFM images of the lower terraces, transition zone, and higher terraces in an etched (211)-oriented SL-G thin film. Along the direction of the grain and through the transition zone starting from the top of the islands, the "double wave" pattern gradually transforms into a "boomerang" pattern. Another region, containing the "droplet" pattern, was also found within the transition zone. Figure 4(c) demonstrates that slicing the SCFT solutions using representative crystallographic planes along the [211] direction in the converged DG unit cell furnishes qualitative matches to these three observed surface patterns.

The morphologies at the terrace boundaries and in the transition zone must minimize interfacial energy subject to the geometrical constraints established by the mismatched adjoining structures. Similar transition zones connecting regions of lower and higher terraces have also been reported in lamellar- and cylinder-forming BCP thin films [33,34,59–63]. For example, lamellar twist boundaries, such as the Scherk surface, join two sets of aligned lamellae that meet orthogonally, thereby accommodating a transition from perpendicular lamellae to parallel lamellar structures in the transition zone [61,62], or an epitaxial transformation to perpendicular cylinders [63] at the boundary of the terraces. Similar behavior of a cylinder-forming SBS triblock copolymer in the transition zone was observed by Knoll et al. [34]. They discovered that perpendicular cylinders or perforated lamellae could accommodate a continuously varying transition zone thickness between terraces possessing parallel cylinders [34]. Orderorder transitions have also been identified. For example, Liu et al. found that a lamellae-to-cylinders transformation can occur at the terrace edges in order to relieve the local chain deformation [63]. Nonetheless, it is reasonable to expect that the three-dimensional BCP structures within transition zones are complicated and could be affected by several factors, including copolymer composition, dispersity, average film thickness, and surface energy at the adjoining interfaces [33,64,65]. It is likely these complications also occur in DGforming BCP thin films, suggesting a direction for significant future work.

Figure 5 examines the local structure near the transition zone in more detail. Figure 5(a) shows AFM images of a (211)-oriented SL-G thin film with surface relief islands ($t_{avg} \sim 9.2d_{211}$). The lateral dimension of the islands is $\sim 5-10~\mu m$. A magnified AFM image of the region between the lower and the higher terraces [blue box in Fig. 5(a)] is shown in Fig. 5(b). (422) termination planes with different directions exist in most of the lower and higher terraces, with a polygrain texture. The transition zone with "boomerang" and "droplet" patterns is marked as a red area in Fig. 5(b). The width of the transition zone was roughly estimated as the difference in the lateral positions of each double-wave pattern to be $\sim 350-400~nm$ ($\sim 7-8~DG$ unit cells). A magnified AFM image of the transition zone [yellow box in Fig. 5(b)] is shown in Fig. 5(c). We discovered that the structural pattern

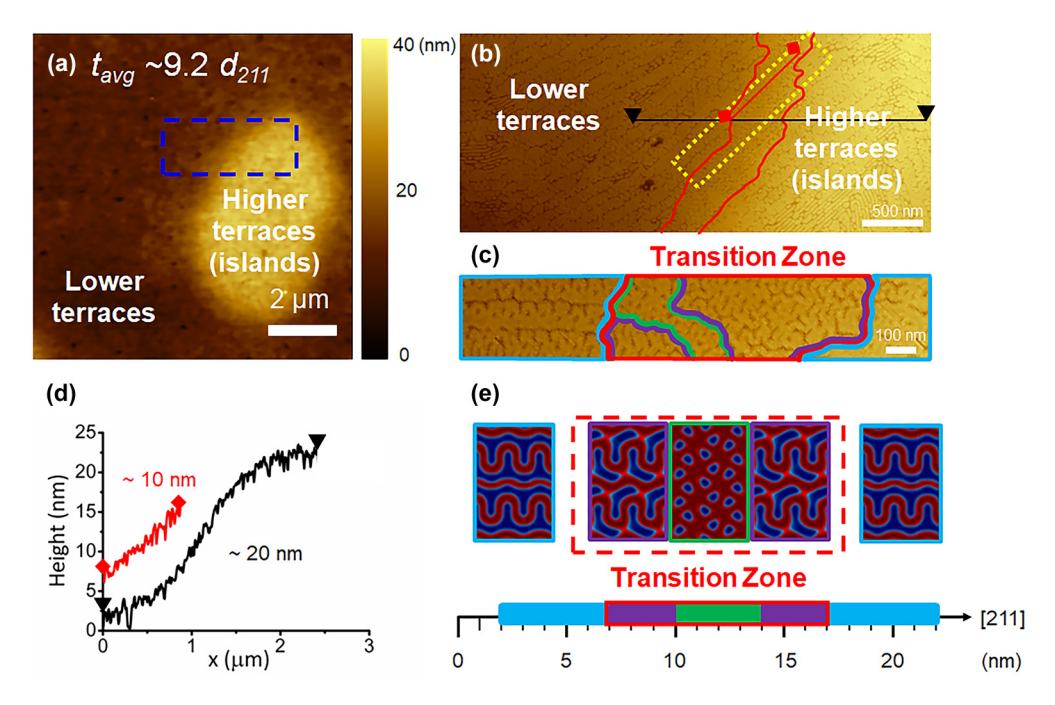


FIG. 5. (a) AFM image of higher terraces formed in an SL-G thin film (after chemical etching of PLA), where the as-cast film thickness was $t_{avg} = 198$ nm $(9.2d_{211})$. (b) AFM image enlargement of the area bounded by the blue box in (a) showing the lower terraces, transition zone (red), and higher terraces in the SL-G thin film. (c) AFM images of the transition zone bounded by the yellow box in panel (b). The regions exhibit three different termination planes consistent with the "double-wave" ($light\ blue$), "boomerang" (purple), and "droplet" (green) patterns. (d) Height profile of the island and transition zone along the line scan in panel (b). The height of the transition zone is approximately 10 ± 1 nm. (e) Simulation results of the termination planes along the [211] direction in the DG unit cell and the corresponding height of the transition zone and surface relief island.

often changes from lower to higher (islands) terraces in the characteristic sequence: "double-wave"→ "boomerang"→ "droplet" → "boomerang" → "double-wave." Based on the SCFT calculations in Fig. S15 (see the Supplemental Material [37]), the sequence of the termination planes along [211] direction could be predicted as (1) "double-wave" to "boomerang" to "droplet" when $0.5 < \tau_{211} < 1$, and (2) "droplet" to "boomerang" to "double-wave" when $0 < \tau_{211} < \tau_{211}$ 0.5, since the termination coordinates $\tau = 0$ and 1 are the same. Thus, the SCFT predictions qualitatively match the experimental results in Fig. 5(c). In some instances, the experimentally observed pattern sequence lacked the "droplet" pattern for unknown reasons. We speculate that this phenomenon might depend on the steepness of the local transition zone along the path of the double-wave pattern (see the different pathways in Fig. S16 [37]).

Figure 5(d) shows the height profiles of the surface terrace island (black) and the transition zone (red). The routes of the step-height measurement are shown in Fig. 5(b). The total step-height of the island from plateau to plateau is 20 ± 1 nm, which is again nearly d_{211} , and this result matches with the height of islands in Fig. 3(h). The height of the transition zone from the end of the double-wave on one terrace to the beginning of the double-wave on the other terrace is also 10 ± 1 nm, that is, close to half of the total step height of the island. This means that a portion of the total step-height (additional ~ 10 nm) must be accommodated by a height transition within the double-wave pattern. Figure 5(e) shows that SCFT results of the domain patterns on crystallographic planes at different points along [211] corresponding in both

pattern sequence and height of the transition zone to those observed in experiments.

IV. CONCLUSIONS

Characterization of the surface relief terraces in DG-forming BCP thin films of a SL-G diblock copolymer revealed the formation of network microdomains oriented with their (211) plans parallel to the underlying substrate, with surface terraces forming depending on the commensurability of the average film thickness with respect to the interplanar distance d_{211} . More explicitly, the terrace heights in these oriented films are almost exactly d_{211} , which is the distance between adjacent (422) planes within the DG morphology. In the broad transitions zones between the terraces, the sequenced observation of "double-wave", "boomerang", and "droplet" patterns is consistent with termination planes along the [211] predicted from SCFT calculations.

The original data to produce figures in this manuscript is available through the Data Repository for the University of Minnesota (DRUM) [66].

ACKNOWLEDGMENTS

We gratefully acknowledge financial support from the National Science Foundation (NSF) through the Materials Research Science and Engineering Center (MRSEC) under Award No. DMR-2011401. Parts of this work were carried out in the Characterization Facility, University of Minnesota, which receives partial support from the NSF through the MR-

SEC (Award No. DMR-2011401) and the NNCI (Award No. ECCS-2025124) programs. This research used synchrotron x-ray resources at the Sector 12-ID-B and 8-ID-E beamlines of the Advanced Photon Source, a U.S. Department of Energy (DOE) Office of Science user facility operated for the DOE Office of Science by Argonne National Laboratory under Contract No. DE-AC02-06CH11357. We gratefully acknowledge

Dr. Z. Jiang and Dr. B. Lee for assistance with 2D-GISAXS and T-SAXS measurements, respectively. We also thank Dr. E. K. McGuinness for helpful discussions.

The manuscript was written through contributions of all authors. All authors have given approval to the final version of the manuscript.

The authors declare no competing financial interest.

- [1] J. N. L. Albert and T. H. Epps, Self-assembly of block copolymer thin films, Mater. Today 13, 24 (2010).
- [2] M. J. Fasolka and A. M. Mayes, Block copolymer thin films: Physics and applications, Annu. Rev. Mater. Res. 31, 323 (2001).
- [3] M. W. Matsen, Thin films of block copolymer, J. Chem. Phys. 106, 7781 (1997).
- [4] P. F. Green and R. Limary, Block copolymer thin films: Pattern formation and phase behavior, Adv. Colloid Interface Sci. 94, 53 (2001).
- [5] M. W. Matsen, Effect of architecture on the phase behavior of AB-Type block copolymer melts, Macromolecules 45, 2161 (2012).
- [6] J. Park and K. I. Winey, Double gyroid morphologies in precise ion-containing multiblock copolymers synthesized via stepgrowth polymerization, Jacs Au 2, 1769 (2022).
- [7] J. A. Dolan, B. D. Wilts, S. Vignolini, J. J. Baumberg, U. Steiner, and T. D. Wilkinson, Optical properties of gyroid structured materials: From photonic crystals to metamaterials, Adv. Opt. Mater. 3, 12 (2015).
- [8] A. M. Urbas, M. Maldovan, P. DeRege, and E. L. Thomas, Bicontinuous cubic block copolymer photonic crystals, Adv. Mater. 14, 1850 (2002).
- [9] M. D. Turner, M. Saba, Q. M. Zhang, B. P. Cumming, G. E. Schroder-Turk, and M. Gu, Miniature chiral beamsplitter based on gyroid photonic crystals, Nat. Photonics 7, 801 (2013).
- [10] Z. S. Gan, M. D. Turner, and M. Gu, Biomimetic gyroid nanostructures exceeding their natural origins, Sci. Adv. 2, e1600084 (2016)
- [11] S. S. Oh, A. Demetriadou, S. Wuestner, and O. Hess, On the origin of chirality in nanoplasmonic gyroid metamaterials, Adv. Mater. 25, 612 (2013).
- [12] L. Li, L. Schulte, L. D. Clausen, K. M. Hansen, G. E. Jonsson, and S. Ndoni, Gyroid nanoporous membranes with tunable permeability, Acs Nano 5, 7754 (2011).
- [13] M. Adachi, A. Okumura, E. Sivaniah, and T. Hashimoto, Incorporation of metal nanoparticles into a double gyroid network texture, Macromolecules 39, 7352 (2006).
- [14] E. J. W. Crossland, M. Kamperman, M. Nedelcu, C. Ducati, U. Wiesner, D. M. Smilgies, G. E. S. Toombes, M. A. Hillmyer, S. Ludwigs, U. Steiner *et al.*, A bicontinuous double gyroid hybrid solar cell, Nano Lett. 9, 2807 (2009).
- [15] F. S. Bates and G. H. Fredrickson, Block copolymer thermodynamics – theory and experiment, Annu. Rev. Phys. Chem. 41, 525 (1990).
- [16] F. S. Bates and G. H. Fredrickson, Block copolymers Designer soft materials, Phys. Today **52**, 32 (1999).
- [17] A. P. Smith, J. F. Douglas, J. C. Meredith, E. J. Amis, and A. Karim, Combinatorial study of surface pattern formation

- in thin block copolymer films, Phys. Rev. Lett. **87**, 015503 (2001).
- [18] K. A. Orso and P. F. Green, Phase behavior of thin film blends of block copolymers and homopolymers: Changes in domain dimensions, Macromolecules 32, 1087 (1999).
- [19] T. L. Morkved and H. M. Jaeger, Thickness-induced morphology changes in lamellar diblock copolymer ultrathin films, Europhys. Lett. 40, 643 (1997).
- [20] H. P. Huinink, J. C. M. Brokken-Zijp, M. A. van Dijk, and G. J. A. Sevink, Asymmetric block copolymers confined in a thin film, J. Chem. Phys. 112, 2452 (2000).
- [21] M. J. Maher, C. M. Bates, G. Blachut, S. Sirard, J. L. Self, M. C. Carlson, L. M. Dean, J. D. Cushen, W. J. Durand, C. O. Hayes et al., Interfacial design for block copolymer thin films, Chem. Mater. 26, 1471 (2014).
- [22] J. W. Hong, J. H. Chang, H. H. Hung, Y. P. Liao, Y. Q. Jian, I. C. Y. Chang, T. Y. Huang, A. Nelson, I. M. Lin, Y. W. Chiang et al., Chain length effects of added homopolymers on the phase behavior in blend films of a symmetric, weakly segregated polystyrene-block-poly(methyl methacrylate), Macromolecules 55, 2130 (2022).
- [23] G. Coulon, T. P. Russell, V. R. Deline, and P. F. Green, Surface-induced orientation of symmetric, diblock copolymers - a secondary ion mass-spectrometry study, Macromolecules 22, 2581 (1989).
- [24] M. A. Vandijk and R. Vandenborg, Ordering phenomena in thin block-copolymer films studied using atomic-force microscopy, Macromolecules 28, 6773 (1995).
- [25] R. Olayo-Valles, S. W. Guo, M. S. Lund, C. Leighton, and M. A. Hillmyer, Perpendicular domain orientation in thin films of polystyrene polylactide diblock copolymers, Macromolecules 38, 10101 (2005).
- [26] Y. Liu, W. Zhao, X. Zheng, A. King, A. Singh, M. H. Rafailovich, J. Sokolov, K. H. Dai, E. J. Kramer, S. A. Schwarz *et al.*, Surface-induced ordering in asymmetric block-copolymers, Macromolecules 27, 4000 (1994).
- [27] A. Menelle, T. P. Russell, S. H. Anastasiadis, S. K. Satija, and C. F. Majkrzak, Ordering of thin eblock copolymer films, Phys. Rev. Lett. 68, 67 (1992).
- [28] A. Horvat, A. Knoll, G. Krausch, L. Tsarkova, K. S. Lyakhova, G. J. A. Sevink, A. V. Zvelindovsky, and R. Magerle, Time evolution of surface relief structures in thin block copolymer films, Macromolecules 40, 6930 (2007).
- [29] L. Tsarkova, A. Knoll, G. Krausch, and R. Magerle, Substrate-induced phase transitions in thin films of cylinder-forming diblock copolymer melts, Macromolecules 39, 3608 (2006).
- [30] R. A. Segalman, H. Yokoyama, and E. J. Kramer, Graphoepitaxy of spherical domain block copolymer films, Adv. Mater. 13, 1152 (2001).

- [31] J. Heier, E. Sivaniah, and E. J. Kramer, Anisotropic coarsening of two-dimensional surface domains in copolymer thin films, Macromolecules **32**, 9007 (1999).
- [32] R. D. Peters, X. M. Yang, and P. F. Nealey, Morphology of thin films of eblock copolymers on surfaces micropatterned with regions of different interfacial energy, Macromolecules 35, 1822 (2002).
- [33] S. Kim, C. M. Bates, A. Thio, J. D. Cushen, C. J. Ellison, C. G. Willson, and F. S. Bates, Consequences of surface neutralization in eblock copolymer thin films, ACS Nano 7, 9905 (2013).
- [34] A. Knoll, A. Horvat, K. S. Lyakhova, G. Krausch, G. J. A. Sevink, A. V. Zvelindovsky, and R. Magerle, Phase behavior in thin films of cylinder-forming block copolymers, Phys. Rev. Lett. 89, 035501 (2002).
- [35] M. Maaloum, D. Ausserre, D. Chatenay, G. Coulon, and Y. Gallot, Edge profile of relief 2D domains at the free-surface of smectic copolymer thin-films, Phys. Rev. Lett. 68, 1575 (1992).
- [36] A. S. Zalusky, R. Olayo-Valles, J. H. Wolf, and M. A. Hillmyer, Ordered nanoporous polymers from polystyrene-polylactide block copolymers, J. Am. Chem. Soc. **124**, 12761 (2002).
- [37] See Supplemental Material at http://link.aps.org/supplemental/ 10.1103/PhysRevMaterials.7.125601 for schematics of polymer synthesis procedure; NMR spectra, SEC chromatograms, DSC data, and TGA analysis of synthesized block copolymer; SEM image and T-SAXS pattern of a DG-forming bulk SL-G sample; SL-G thin film preparation procedure; SL-G thin film thickness measurement by ellipsometry; OM, SEM, AFM images and 2D GISAXS patterns of SL-G thin films; visualizations of different termination planes along the [211] direction in an ideal DG unit cell derived from a converged SCFT solution.
- [38] M. G. Karavolias, J. B. Elder, E. M. Ness, and M. K. Mahanthappa, Order-to-disorder transitions in lamellar melt self-assembled core–shell bottlebrush polymers, ACS Macro Lett. 8, 1617 (2019).
- [39] J. D. Cushen, L. Wan, G. Pandav, I. Mitra, G. E. Stein, V. Ganesan, R. Ruiz, C. Grant Willson, and C. J. Ellison, Ordering poly(trimethylsilyl styrene-block-D,L-lactide) block copolymers in thin films by solvent annealing using a mixture of domain-selective solvents, J. Polym. Sci. Part B 52, 36 (2014).
- [40] C. Cummins, P. Mokarian-Tabari, J. D. Holmes, and M. A. Morris, Selective etching of polylactic acid in poly(styrene)-block-poly(D,L)lactide diblock copolymer for nanoscale patterning, J. Appl. Polym. Sci. 131, 40798 (2014).
- [41] Z. Jiang, GIXSGUI: A MATLAB toolbox for grazing-incidence X-ray scattering data visualization and reduction, and indexing of buried three-dimensional periodic nanostructured films, J. Appl. Crystallogr. 48, 917 (2015).
- [42] A. Arora, J. Qin, D. C. Morse, K. T. Delaney, G. H. Fredrickson, F. S. Bates, and K. D. Dorfman, Broadly accessible selfconsistent field theory for block polymer materials discovery, Macromolecules 49, 4675 (2016).
- [43] https://github.com/kdorfmanUMN/polymer_visual.
- [44] H. Mao and M. A. Hillmyer, Macroscopic samples of polystyrene with ordered three-dimensional nanochannels, Soft Matter 2, 57 (2006).
- [45] D. J. Chen, Y. M. Gong, H. Y. Huang, T. B. He, and F. J. Zhang, Competition of lamellar orientation in thin films of a symmetric poly(styrene)-b-poly(L-lactide) diblock copolymer in melt state, Macromolecules 40, 6631 (2007).

- [46] P. Mansky, Y. Liu, E. Huang, T. P. Russell, and C. Hawker, Controlling polymer-surface interactions with random copolymer brushes, Science **275**, 1458 (1997).
- [47] S. Ham, C. Shin, E. Kim, D. Y. Ryu, U. Jeong, T. P. Russell, and C. J. Hawker, Microdomain orientation of PS-b-PMMA by controlled interfacial interactions, Macromolecules 41, 6431 (2008).
- [48] C. M. Bates, T. Seshimo, M. J. Maher, W. J. Durand, J. D. Cushen, L. M. Dean, G. Blachut, C. J. Ellison, and C. G. Willson, Polarity-Switching top coats enable orientation of sub-10-nm block copolymer domains, Science 338, 775 (2012).
- [49] M. W. Matsen, Polydispersity-induced macrophase separation in diblock copolymer melts, Phys. Rev. Lett. **99**, 148304 (2007).
- [50] N. A. Lynd, A. J. Meuler, and M. A. Hillmyer, Polydispersity and block copolymer self-assembly, Prog. Polym. Sci. **33**, 875 (2008).
- [51] Y. H. Wu, T. Y. Lo, M. S. She, and R. M. Ho, Morphological evolution of gyroid-forming block copolymer thin films with varying solvent evaporation rate, ACS Appl. Mater. Interfaces 7, 16536 (2015).
- [52] J. Jung, J. Lee, H. W. Park, T. Chang, H. Sugimori, and H. Jinnai, Epitaxial phase transition between double gyroid and cylinder phase in diblock copolymer thin film, Macromolecules 47, 8761 (2014).
- [53] S. R. Nowak, K. K. Lachmayr, K. G. Yager, and L. R. Sita, Stable thermotropic 3D and 2D double gyroid nanostructures with sub-2-nm feature size from scalable sugar-polyolefin conjugates, Angew. Chem. Int. Ed. 60, 8710 (2021).
- [54] W. B. Bai, A. F. Hannon, K. W. Gotrik, H. K. Choi, K. Aissou, G. Liontos, K. Ntetsikas, A. Alexander-Katz, A. Avgeropoulos, and C. A. Ross, Thin film morphologies of bulk-gyroid polystyrene-block-polydimethylsiloxane under solvent vapor annealing, Macromolecules 47, 6000 (2014).
- [55] J. Jung, H. W. Park, S. Lee, H. Lee, T. Chang, K. Matsunaga, and H. Jinnai, Effect of film thickness on the phase behaviors of diblock copolymer thin film, Acs Nano 4, 3109 (2010).
- [56] S. Jo, T. Jun, H. I. Jeon, S. Seo, H. Kim, S. Lee, and D. Y. Ryu, Optical reflection from unforbidden diffraction of block copolymer templated gyroid films, Acs Macro Letters 10, 1609 (2021).
- [57] S. Jo, H. Park, T. Jun, K. Kim, H. Jung, S. Park, B. Lee, S. Lee, and D. Y. Ryu, Symmetry-breaking in double gyroid block copolymer film, Acta Crystallogr. A 77, C137 (2021).
- [58] V. N. Urade, T. C. Wei, M. P. Tate, J. D. Kowalski, and H. W. Hillhouse, Nanofabrication of double-gyroid thin films, Chem. Mater. 19, 2382 (2007).
- [59] K. Binder, Surface effects on polymer blends and block-copolymer melts Theoretical concepts of surface enrichment, surface-induced phase-separation and ordering, Acta Polym. 46, 204 (1995).
- [60] J. A. Dolan, R. Dehmel, A. Demetriadou, Y. B. Gu, U. Wiesner, T. D. Wilkinson, I. Gunkel, O. Hess, J. Baumberg, U. Steiner et al., Metasurfaces atop metamaterials: Surface morphology induces linear dichroism in gyroid optical metamaterials, Adv. Mater. 31, e1803478 (2019).
- [61] B. L. Carvalho and E. L. Thomas, Morphology of steps in terraced block-copolymer films, Phys. Rev. Lett. 73, 3321 (1994).
- [62] S. P. Gido, J. Gunther, E. L. Thomas, and D. Hoffman, Lamellar diblock copolymer grain-boundary morphology. 1. Twist boundary characterization, Macromolecules **26**, 4506 (1993).

- [63] Y. Liu, M. H. Rafailovich, J. Sokolov, S. A. Schwarz, and S. Bahal, Effects of surface tension on the dislocation structures of diblock copolymers, Macromolecules 29, 899 (1996).
- [64] K. S. Lyakhova, A. Horvat, A. V. Zvelindovsky, and G. J. A. Sevink, Dynamics of terrace formation in a nanostructured thin block copolymer film, Langmuir 22, 5848 (2006).
- [65] K. S. Lyakhova, G. J. A. Sevink, A. V. Zvelindovsky, A. Horvat, and R. Magerle, Role of dissimilar interfaces in thin films of cylinder-forming block copolymers, J. Chem. Phys. 120, 1127 (2004).
- [66] S.-M. Yang, J. Oh, B. Magruder, H. J. Kim, K. D. Dorfman, M. K. Mahanthappa, and C. J. Ellison, data for "Surface relief terraces in double gyroid-forming polystyrene-block-polylactide thin films", University of Minnesota, doi:10.13020/qc9e-qc68.